Biophysical Journal, Volume *113*

Supplemental Information

Quantitative Deformability Cytometry: Rapid, Calibrated Measurements of Cell Mechanical Properties

Kendra D. Nyberg, Kenneth H. Hu, Sara H. Kleinman, Damir B. Khismatullin, Manish J. Butte, and Amy C. Rowat

SUPPLEMENTAL INFORMATION

Viscoelastic Models. To measure the mechanical properties of cells from individual creep trajectories, we evaluate the quality of fit of standard viscoelastic models. The Maxwell, Kelvin-Voigt, and Standard Linear Solid models are represented by combinations of springs and dashpots. Similar to the springs and dashpot models, Power Law Rheology (PLR) provides a measure of elastic and viscous components of cells, whereby the power law exponent, or fluidity, reflects the viscous behavior (1). While we show in this study that PLR minimizes the residuals for HL-60 cells, certain cell types may be better described using other viscoelastic models (2).

Maxwell	$J_M(t) = k_1 + k_2 t$	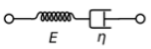
Kelvin-Voigt	$J_{KV}(t) = k_1(1 - e^{k_2 t})$	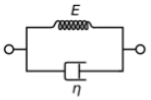
Standard Linear Solid	$J_{SLS}(t) = \frac{1}{k_1} e^{-k_2 k_3 t} + \frac{k_1 + k_2}{k_1 k_2}(1 - e^{-k_2 k_3 t})$	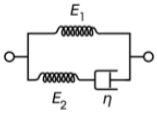
Power Law Rheology	$J_{PLR}(t) = k_1 t^{\beta}$	

Data analysis. Analysis of q-DC data is performed using MATLAB (MathWorks, Natick, MA, USA). The video processing code is available on Github. Median residuals and corresponding confidence intervals are determined by bootstrapping 5000 iterations of theoretical fits to single cell data. Residual fits are determined using the least squares method. A value reported in the text as 'X ± Y' is the bootstrapped median, 'X', using bootstrapped resampling with the confidence interval, '2*Y'. This bootstrapping method is also employed for determining β values, as well as the interquartile ranges. To compare the distributions of q-DC outputs between cell lines and drug treatments, we apply the pairwise, nonparametric Mann-Whitney U statistical test as most q-DC parameters are not normally distributed. Density scatter plots are created using the dscatter function (R. Henson, Mathworks File Exchange). We assess the strength of correlations between q-DC outputs by determining Pearson's correlation coefficients for pairs of parameters.

SUPPLEMENTAL TABLES

S. Table 1. Viability of HL-60 cells after pharmacological perturbations. Cell viability is determined using a Trypan blue assay.

Treatment	Viability
DMSO (Control)	97.6 ± 0.8%
Cytochalasin D	86.4 ± 2.7%
Blebbistatin	84.5 ± 1.1%
Jasplakinolide	90.3 ± 2.3%

S. Table 2. E_a and β values from q-DC measurements. The median E_a and β are determined by 1000 bootstrapped samples from the density-gated q-DC data. Error represents the corresponding confidence intervals.

Geometry w x h (μm^2)	$P_{applied}$ (kPa)	Cell Line	Treatment	E_a (kPa)	σ_{IQR_Ea}	β	σ_{IQR_β}
5 x 5	28	HL-60	DMSO (Control)	0.53 ± 0.04	0.35 ± 0.06	0.29 ± 0.02	0.25 ± 0.03
5 x 5	28	HL-60	Cytochalasin D	0.52 ± 0.06	0.40 ± 0.08	0.29 ± 0.02	0.28 ± 0.05
5 x 5	28	HL-60	Blebbistatin	0.39 ± 0.05	0.46 ± 0.08	0.34 ± 0.03	0.33 ± 0.04
5 x 5	28	HL-60	Jasplakinolide	0.55 ± 0.07	0.30 ± 0.06	0.27 ± 0.03	0.27 ± 0.06
5 x 10	14	HL-60	-	0.52 ± 0.10	0.66 ± 0.09	0.49 ± 0.04	0.22 ± 0.04
5 x 10	34	HL-60	-	0.99 ± 0.08	0.49 ± 0.06	0.46 ± 0.02	0.19 ± 0.03
5 x 10	69	HL-60	-	1.4 ± 0.21	0.70 ± 0.16	0.39 ± 0.03	0.27 ± 0.05
9 x 10	28	HL-60	-	0.15 ± 0.03	0.86 ± 0.18	0.50 ± 0.04	0.28 ± 0.05
9 x 10	69	MCF-7	-	2.1 ± 0.14	0.41 ± 0.09	0.28 ± 0.01	0.19 ± 0.03
9 x 10	69	MDA-MB-231	-	0.80 ± 0.19	0.84 ± 0.10	0.40 ± 0.03	0.33 ± 0.04

S. Table 3. *E* and *β* values from literature.

Cell Line	Method	Elastic Modulus *E*	Fluidity *β*	Ref.
HL-60	AFM	855 ± 670 Pa	-	(3)
	OS	34.5 ± 36.5 Pa	0.65 ± 0.5	(2)
		23.8 ± 7.4 Pa	0.82 ± 0.2	(4)
MCF-7	AFM	0.285 ± 0.127 kPa	-	(5)
		1.04 ± 0.27 kPa	-	(6)
		50.2 ± 38.5 kPa to 87.3 ± 47.8 kPa	-	(7)
		0.5 ± 0.1 to 28 ± 12 kPa	-	(8)
		0.420 - 1.210 kPa	-	(9)
		0.25 ± 0.02 kPa	0.25 ± 0.02	(10)
MDA-MB-231	AFM	0.277 ± 0.063 kPa	-	(5)
		0.63 ± 0.21 kPa	-	(6)
		28.7 ± 26.1 kPa to 55.6 ± 20.1 kPa	-	(7)
		0.3 ± 0.1 kPa to 25 ± 13 kPa	-	(8)
		0.69 ± 0.06 kPa	0.22 ± 0.01	(10)
		0.20 - 0.30 kPa to 0.19-0.23 kPa	-	(11)
	DC	0.58 kPa	0.27	(12)

S. Table 4. Calibration for applied stress in varying device geometries. The calibration factors are determined by the threshold pressure method. Utilizing agarose calibration particles, we are able to determine the applied stress at the constriction region.

Geometry w x h (μm^2)	*A*	$P_{applied}$ (kPa)	σ (Pa)
5x5	0.021 ± 0.002	28	570 ± 50
5x10	0.070 ± 0.018	14	960 ± 250
		34	2400 ± 630
		69	4800 ± 1300
9x10	0.032 ± 0.002	34	1100 ± 60

SUPPLEMENTAL FIGURES

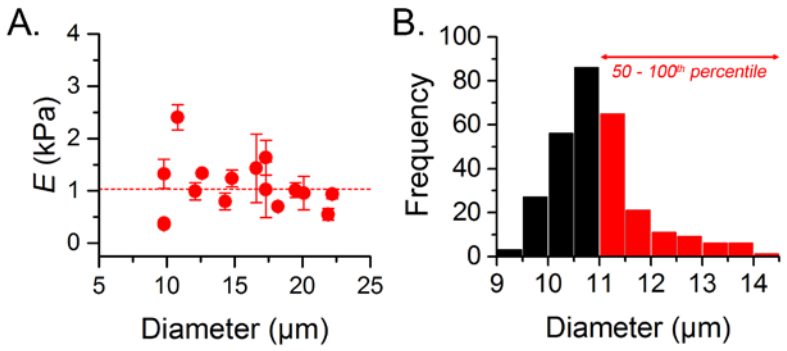

S. Fig. 1. Agarose calibration particles exhibit size-independent elastic moduli. (*A*) Elastic modulus of particles composed of 1.5% (w/w) agarose as a function of particle diameter as measured by AFM. Data represents the mean ± standard deviation for each particle probed 2-5 times. The red dotted line illustrates the average elastic modulus. Data collected over two independent experiments (N = 15). (*B*) Distribution of diameters for particles composed of 1.5% (w/w) agarose as they transit through 5 μm x 5 μm constrictions. The 50^{th} – 100^{th} percentile of sizes are considered to determine the median maximum strain at the threshold pressure conditions as depicted by the red bars (N = 220).

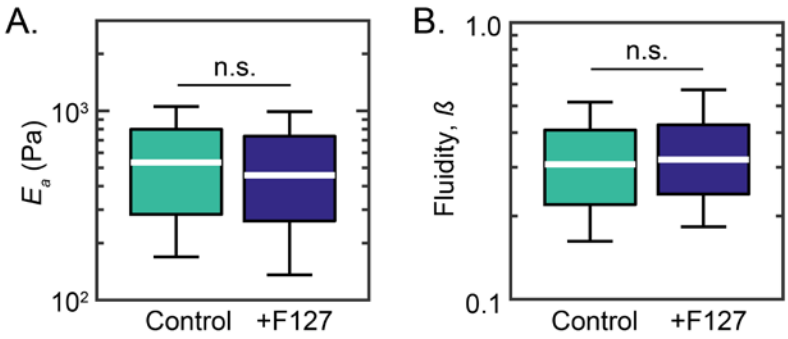

S. Fig. 2. Effects of surfactant on cell mechanotyping. Apparent elastic modulus E_a and fluidity β values of HL-60 cells treated with pluronic F-127 during transit through microfluidic constrictions. White lines represent the median E_a and β. Boxes represent the interquartile ranges and whiskers represent the 10^{th} – 90^{th} percentiles (N > 500). The Mann-Whitney U test is used to evaluate statistical significance. n.s. denotes $p \geq 0.05$.

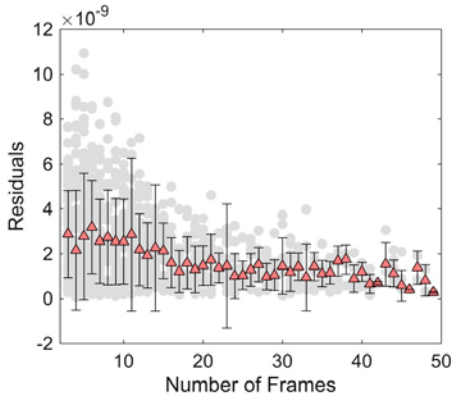

S. Fig. 3. Residuals of PLR creep fit depends on frame number. Scatter plot of the residuals per frame for HL-60 cells. The gray dots represent the residuals for individual cells. The orange triangles illustrate the median residual for each number of frames. The error bars represent the interquartile range. N = 550. There exists a trade-off between the quality of PLR fitting and the dynamic range of q-DC. By minimizing the required number of frames for creep trajectories, the dynamic range extends to sample longer deformation timescales within a population of cells.

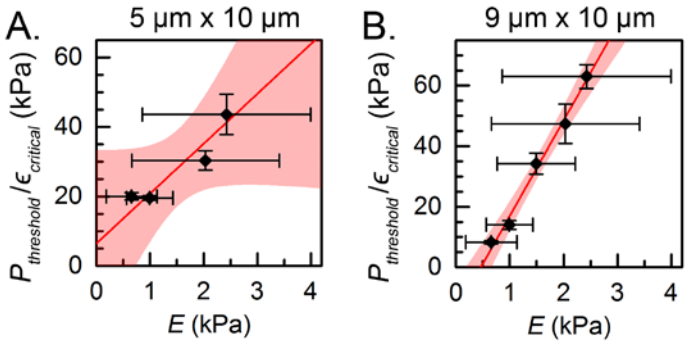

S. Fig. 4. Threshold transit conditions for characterizing applied stress in microfluidic constrictions. Threshold applied pressures in the (*A*) 5 μm x 10 μm and (*B*) 9 μm x 10 μm microfluidic device geometries for calibration particles with a range of elastic moduli, 0.6 – 2.4 kPa. X-error bars represent the standard deviation of the elastic modulus as determined by AFM. Y-error bars represent the standard deviation of the pressure-to-particle strain ratio. The red line is the linear fit; the red shaded region illustrates the 95% confidence interval of the linear fit. The inverse of the slope characterizes the applied pressure-to-stress scaling factor. N > 650 for strain measurements at each threshold condition.

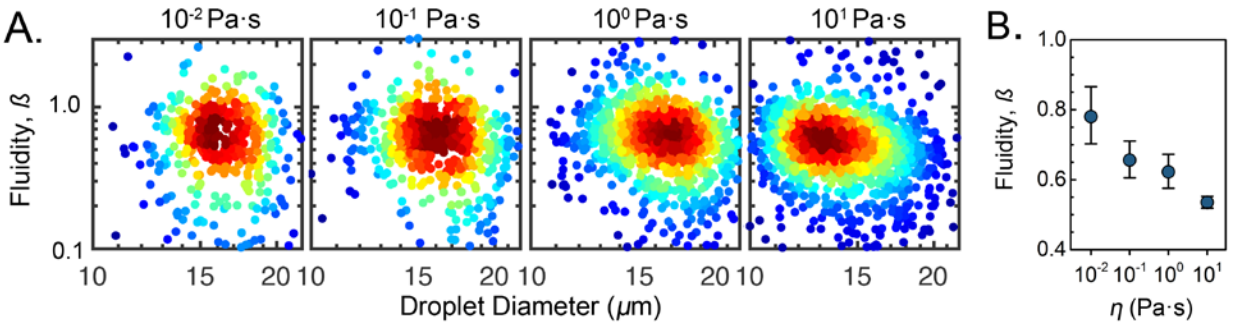

S. Fig. 5. Power law exponent for oil particles. (*A*) Validation of power law rheology using oil-in-water emulsion droplets made with silicone oils of varying viscosities. Power law exponents, β, for oil droplets calculated by the least-squares fit of deformation trajectories with power law rheology model. Density scatter plots represent β as a function of droplet size. Each dot represents a single cell. Color represents the density of points. White diamonds show the highest density of points. N > 500 oil droplets. (*B*) Bootstrapped median values of β for droplets of silicone oils. Error bars denote the bootstrapped confidence intervals.

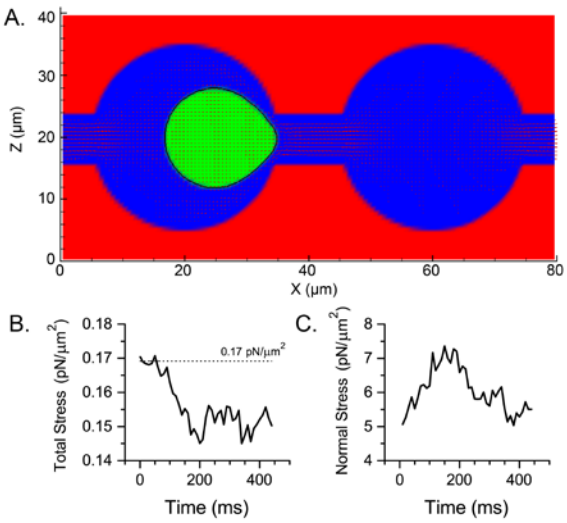

S. Fig. 6. Numerical simulations of single cells deforming through a constriction. (*A*) Simulation of a cell deforming through a micron-scale constriction. Shown here is a representative cell with a diameter of 16.3 μm transiting through a constriction with a width of 8.1 μm; the cell-to-pore size ratio is 2. The red arrows represent the flow vector field. (*B-C*) The total hydrodynamic stress (B) and normal stress (C) acting on a cell as it transits through a constriction; cell-to-pore size ratio is 1. When the cell is transiently occluding the pore, there are positive normal forces that deform the cell. As the transiting cell continually deforms through the constriction, there is also a drop in hydrodynamic force: according to Stokes' law, the hydrodynamic force is proportional to the cell velocity and thus a decrease in the cell velocity leads to a decrease in the hydrodynamic force. The black dotted line represents the baseline hydrodynamic stress acting on the cell before it reaches the constriction.

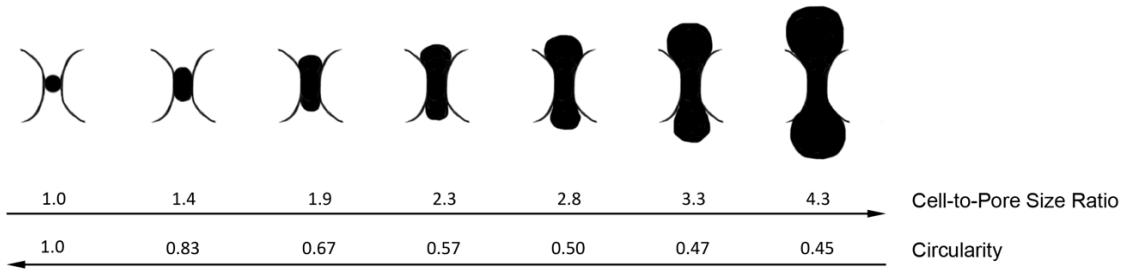

S. Fig. 7. Shape library. Graphic representation of shape changes in cells with a range of sizes during transit through a microfluidic constriction. Cell-to-pore size ratio is determined by the ratio between the unconstrained cell diameter and the width of the constriction, where the unconstrained cell diameter is calculated as the diameter of a perfect circle with an area of the cell's projected area.

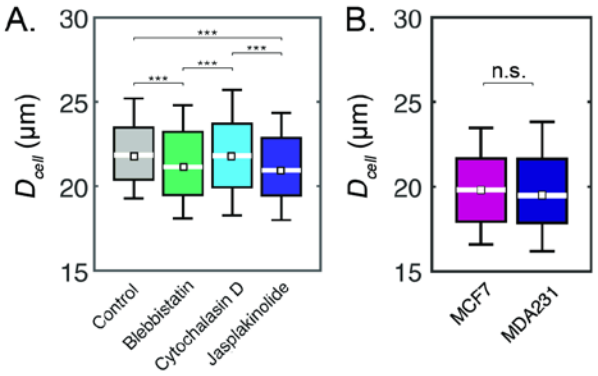

S. Fig. 8. Size distributions of HL-60 cells treated with cytoskeletal-perturbing drugs and breast cancer cell lines. Box plots represent the cell diameters as determined by brightfield imaging during q-DC measurements. White lines represent the median, boxes represent the interquartile ranges, whiskers represent the 10th and 90th percentiles, and white squares represent the bootstrapped median.

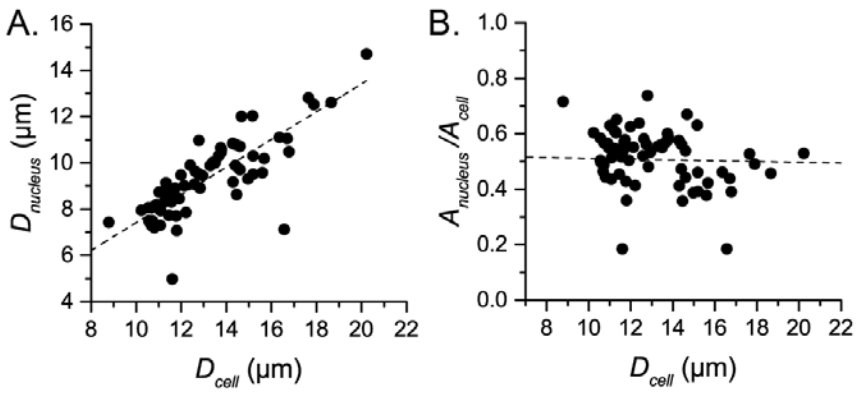

S. Fig. 9. Cell and nuclear size in HL-60 cells. Scatter plots of (*A*) nuclear diameter versus cell diameter and (*B*) nuclear-to-cell area ratio versus cell diameter for HL-60 cells. Cells are stained with Hoechst and Calcein AM; thereafter, samples are imaged via confocal microscopy. Each point represents data for a single cell. Black dotted line shows linear fit to the data.

SUPPLEMENTAL BIBLIOGRAPHY

1. Fabry, B., G.N. Maksym, J.P. Butler, M. Glogauer, D. Navajas, and J.J. Fredberg. 2001. Scaling the microrheology of living cells. Phys. Rev. Lett. 87: 148102.
2. Ekpenyong, A.E., G. Whyte, K. Chalut, S. Pagliara, F. Lautenschläger, C. Fiddler, S. Paschke, U.F. Keyser, E.R. Chilvers, and J. Guck. 2012. Viscoelastic Properties of Differentiating Blood Cells Are Fate- and Function-Dependent. PLoS One. 7.
3. Rosenbluth, M.J., W.A. Lam, and D.A. Fletcher. 2006. Force microscopy of nonadherent cells: a comparison of leukemia cell deformability. Biophys. J. 90: 2994–3003.
4. Chan, C.J., A.E. Ekpenyong, S. Golfier, W. Li, K.J. Chalut, O. Otto, J. Elgeti, J. Guck, and F. Lautenschläger. 2015. Myosin II Activity Softens Cells in Suspension. Biophys. J. 108: 1856–1869.
5. Corbin, E.A., F. Kong, C.T. Lim, W.P. King, and R. Bashir. 2015. Biophysical properties of human breast cancer cells measured using silicon MEMS resonators and atomic force microscopy. Lab Chip. 15: 839–847.
6. Omidvar, R., M. Tafazzoli-Shadpour, M.A. Shokrgozar, and M. Rostami. 2014. Atomic force microscope-based single cell force spectroscopy of breast cancer cell lines: an approach for evaluating cellular invasion. J. Biomech. 47: 3373–3379.
7. Coceano, G., M.S. Yousafzai, W. Ma, F. Ndoye, L. Venturelli, I. Hussain, S. Bonin, J. Niemela, G. Scoles, D. Cojoc, and E. Ferrari. 2016. Investigation into local cell mechanics by atomic force microscopy mapping and optical tweezer vertical indentation. Nanotechnology. 27: 65102.
8. Calzado-Martín, A., M. Encinar, J. Tamayo, M. Calleja, A. San Paulo, A. Calzado-Martin, M. Encinar, J. Tamayo, M. Calleja, and A. San Paulo. 2016. Effect of actin organization on the stiffness of living breast cancer cells revealed by peak-force modulation atomic force microscopy. ACS Nano. 10: 3365–3374.
9. Li, Q.S., G.Y.H. Lee, C.N. Ong, and C.T. Lim. 2008. AFM indentation study of breast cancer cells. Biochem. Biophys. Res. Commun. 374: 609–613.
10. Rother, J., H. Noding, I. Mey, and A. Janshoff. 2014. Atomic force microscopy-based microrheology reveals significant differences in the viscoelastic response between malign and benign cell lines. Open Biol. 4: 140046.
11. Agus, D.B., J.F. Alexander, W. Arap, S. Ashili, J.E. Aslan, R.H. Austin, V. Backman, K.J. Bethel, R. Bonneau, W.-C. Chen, C. Chen-Tanyolac, N.C. Choi, S.A. Curley, M. Dallas, D. Damania, P.C.W. Davies, P. Decuzzi, L. Dickinson, L. Estevez-Salmeron, V. Estrella, M. Ferrari, C. Fischbach, J. Foo, S.I. Fraley, C. Frantz, A. Fuhrmann, P. Gascard, R.A. Gatenby, Y. Geng, S. Gerecht, R.J. Gillies, B. Godin, W.M. Grady, A. Greenfield, C. Hemphill, B.L. Hempstead, A. Hielscher, W.D. Hillis, E.C. Holland, A. Ibrahim-Hashim, T. Jacks, R.H. Johnson, A. Joo, J.E. Katz, L. Kelbauskas, C. Kesselman, M.R. King, K. Konstantopoulos, C.M. Kraning-Rush, P. Kuhn, K. Kung, B. Kwee, J.N. Lakins, G. Lambert, D. Liao, J.D. Licht, J.T. Liphardt, L. Liu, M.C. Lloyd, A. Lyubimova, P. Mallick, J. Marko, O.J.T. McCarty, D.R. Meldrum, F. Michor, S.M. Mumenthaler, V. Nandakumar, T. V O'Halloran, S. Oh, R. Pasqualini, M.J. Paszek, K.G. Philips, C.S. Poultney, K. Rana, C.A. Reinhart-King, R. Ros, G.L. Semenza, P. Senechal, M.L. Shuler, S. Srinivasan, J.R. Staunton, Y. Stypula, H. Subramanian, T.D. Tlsty, G.W. Tormoen, Y. Tseng, A. van Oudenaarden, S.S. Verbridge, J.C. Wan, V.M. Weaver, J. Widom, C. Will, D. Wirtz, J. Wojtkowiak, and P.-H. Wu. 2013. A physical sciences network characterization of non-tumorigenic and metastatic cells. Sci. Rep. 3: 1449.
12. Lange, J.R., J. Steinwachs, T. Kolb, L.A. Lautscham, I. Harder, G. Whyte, and B. Fabry. 2015. Microconstriction Arrays for High-Throughput Quantitative Measurements of Cell Mechanical Properties. Biophys. J. 109: 26–34.